LAWRENCE
LIVERMORE
NATIONAL
LABORATORY

# Analyses of U metal for H, C and O

P. K. Weber, J. E. Matzel, I. D. Hutcheon

December 5, 2012

**Disclaimer**

This document was prepared as an account of work sponsored by an agency of the United States government. Neither the United States government nor Lawrence Livermore National Security, LLC, nor any of their employees makes any warranty, expressed or implied, or assumes any legal liability or responsibility for the accuracy, completeness, or usefulness of any information, apparatus, product, or process disclosed, or represents that its use would not infringe privately owned rights. Reference herein to any specific commercial product, process, or service by trade name, trademark, manufacturer, or otherwise does not necessarily constitute or imply its endorsement, recommendation, or favoring by the United States government or Lawrence Livermore National Security, LLC. The views and opinions of authors expressed herein do not necessarily state or reflect those of the United States government or Lawrence Livermore National Security, LLC, and shall not be used for advertising or product endorsement purposes.

This work performed under the auspices of the U.S. Department of Energy by Lawrence Livermore National Laboratory under Contract DE-AC52-07NA27344.

# Analyses of U metal for H, C and O

Peter Weber, Jenny Matzel, Ian Hutcheon

Chemical Sciences Division

December 4, 2012

## Summary

We investigated the distribution of H, C and O in U metal using high-resolution secondary ion mass spectrometry. We made the following findings:

- H co-occurred with C in both large (> 3 $\mu$m) and small (<1 $\mu$m) inclusions.

- The large inclusions are uranium carbide ($UC_x$) crystals, which are abundant and obvious in this sample. These inclusions generally have H-rich rims and lower but significant H abundance in their interiors.

- The small inclusions are either isometric (point-like) or linear. They are heterogeneously distributed and locally aggregated in the sample, with:

    - As many as ~100 in a 100 x 100 $\mu m^2$ area (1 instance)
    - As few as zero (1 instance)
    - A median abundance of 10 per 100 x 100 $\mu m^2$ and an average abundance of 27 per 100 x 100 $\mu m^2$ (N=6).

- The ratio of H to C varied in the inclusions. The rims of the large inclusions tended to have the highest $H^-/C^-$ ion ratios. $H^-$ and $C^-$ count rates largely track each other in the small inclusions. The small inclusions tend to have $H^-/C^-$ ratios almost 100x higher than the interiors of the large inclusions, but less than the rims of the large inclusions.

    - Based on $H^-/C^-$ ratio data, it is likely that the small inclusions and the rims are a different phase or mixture of phases from the $UC_x$ crystals. Given their higher H content, they likely include $UH_3$. Given their significant C content, they likely also contain $UC_x$. Quantification of H content, X-ray and electron diffraction data could provide more conclusive data.

- We make initial estimates of H abundance relative to C based on published sensitivity factors for H and C in silicon, but our estimates are highly uncertain because of the unusually high yield of the $C_2^-$ dimer from the $UC_x$ crystal relative to $C^-$. We attempt to correct for the abundance of all C species, but the resulting estimates must be taken as very preliminary. Using our preliminary correction factors, the H/C ratio in the $UC_x$

crystals is ~0.004 compared to ~0.2 in the small inclusions and higher in the rims. We estimate that the concentration of H in the $UC_x$ crystals is ~0.3% atom-per-atom or ~10 ppm by weight, which seems much too high given the abundance of $UC_x$ crystals and that H is not just in the $UC_x$ crystals.

- Given the seeming failure of the preliminary correction factors for H in the $UC_x$ crystals, it is not worth reporting the estimated H/C atom ratios in the small inclusions and rims.

- Generally both large (> 3 $\mu$m) and small (<1 $\mu$m) inclusions resulted in distinct topographic features after sputtering because they sputter more slowly than the surrounding U metal, and therefore NanoSIMS could be used for locating inclusions that could then be studied by other methods.

In addition to these observations concerning H, we also found:

- O was at background levels in most H-rich inclusions after surface adsorbed O was removed during pre-analysis sputtering.

- There were occasional O-rich inclusions in the large $UC_x$ crystals. Some of these O-rich inclusions were high in H.

- The initial estimate for the sputter rate for U metal with 16 kV $Cs^+$ is $1.28\pm0.08\cdot\mu m^2$ nm $pA^{-1}\cdot s^{-1}$ (average ± standard error) and $0.66\pm0.03\cdot\mu m^2$ nm $pA^{-1}\cdot s^{-1}$ for $UC_x$.

## Introduction

The reaction of oxygen with uranium hydride (UH₃) in uranium metal is thought to be an important cause of corrosion. UH₃ is expected to occur in U metal because hydrogen from gaseous H and water permeates the molten U during casting, and hydrogen concentrations greater than 0.1 ppma (μmol H/mol U) exceed the solubility limit for hydrogen in U metal and therefore should lead to the formation of UH₃ (Powell 2007). One goal of this work is to test for UH₃ and otherwise identify the phase or phases in U metal that contain H.

Previous studies have suggested that UH₃ occurs as micron or sub-micron inclusions within the U metal and at grain boundaries (personal communication, W. Siekhaus). Assuming 1 ppma H in U metal and 1 micron diameter inclusions, the density of inclusions would be on the order of 200 sites per square millimeter under this hypothesis, or ~2 in a 100 x 100 μm² area (Fig. 1). By contrast, the imaging studies suggest that UH₃ inclusions occur at significantly higher density. Another goal of this work is to provide data on the density and distribution of H in U metal.

In this study, we provide data on the distribution of H, C and O in a U metal sample. A significant challenge of this work is that the surface of U metal rapidly oxidizes. Our goal was to sputter through the surface oxidation into the native metal to enable imaging of the hydrogen distribution. We perform this sputtering and analysis with a high-resolution secondary ion mass spectrometry (SIMS) instrument, the CSD Cameca NanoSIMS 50. SIMS uses a primary ion beam to sputter solid samples, generating secondary ions, which are analyzed in the secondary ion mass spectrometer. H through Pu can be detected and quantified. The NanoSIMS is a state-of-the-art SIMS instrument that combines high sensitivity (up to 1 in 20 atoms detected per sputtered), high specificity (flat top peaks with M/ΔM up to 10,000) and high lateral resolution (as good as 50 nm).
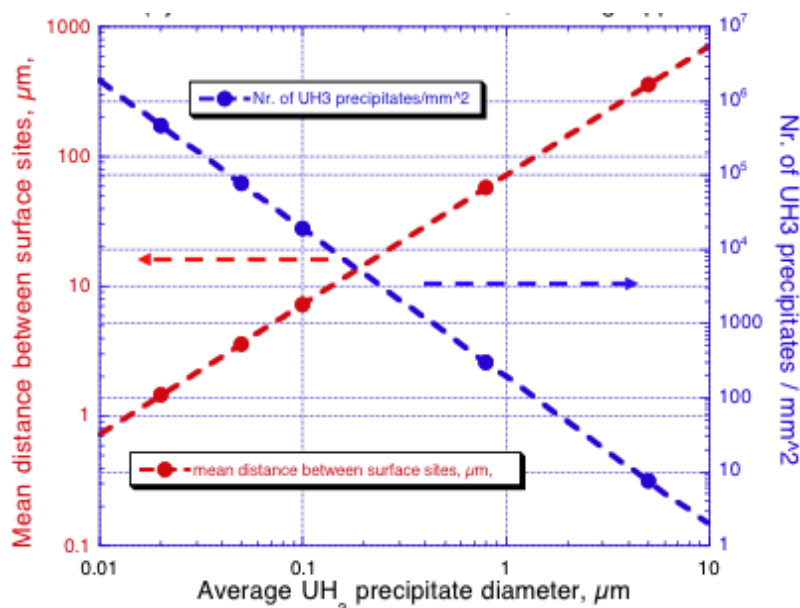


Figure 1. Nomogram of the hypothesized density of UH₃ inclusions in a U metal sample with 1 ppma H (courtesy of W. Siekhaus).

**Methods**

We were provided a ¼ inch diameter disk of polished U metal with 1 ppma H. Three sub-regions had been sputtered with Ga$^+$ in the LLNL focused ion beam (FIB) instrument. The disk was imaged by light microscopy (Fig. 2) and inserted into the CSD NanoSIMS 50. Optical microscopy showed that the U metal sample contained abundant micron to tens-of-micron scale inclusions, which we hypothesized to be UC$_x$ crystals. Therefore, we included C detection in our analyses.
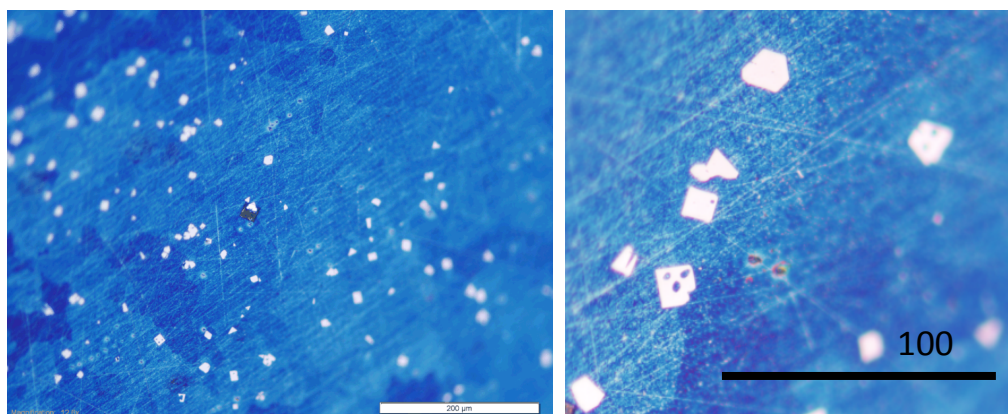


Figure 2. Optical micrographs of U metal, in which UC$_x$ inclusions appear as bright crystals. Note the dark square of the FIB sputtered crater in the left hand micrograph.

100

In the NanoSIMS, pre-analysis sputtering and imaging analysis were performed with a 16kV Cs$^+$ primary ion beam. Pre-analysis sputtering was performed with ~370pA or ~1nA Cs$^+$ over 40 x 40 $\mu m^2$ to 110 x 110 $\mu m^2$ areas for several hours to overnight. The goal of pre-analysis sputtering was to remove surface oxidation to a depth greater than 1$\mu m$ in depth. Imaging analysis was performed with a high primary beam current (15pA Cs$^+$) resulting in relatively low lateral resolution images (<400nm beam diameter as opposed to the ~50 nm beam diameter achieved at lower beam current). This high beam current was used to enable imaging of large areas relatively rapidly and to reduce the influence of vacuum H$_2$O on H and O secondary ion imaging. Secondary ion images were typically 90 x 90 $\mu m^2$ to 50 x 50 $\mu m^2$ with 256 x 256 pixel rasters; these settings were compromises between analysis speed and raster area coverage.

The secondary ion mass spectrometer was tuned for ~3000 M/$\Delta$M with flat top peaks. Secondary ion analysis was performed by magnetic peak switching with H$^-$ detected with one magnetic field, and $^{12}$C$^-$ and $^{16}$O$^-$ detected with a second magnetic field. Secondary electrons were also detected for sample imaging. An issue with vertical detector alignment resulted in attenuated detection of $^{16}$O$^-$ and potentially $^{12}$C$^-$, but the distribution of the elements should be representative. After discussions with the NanoSIMS manufacture, we identified the problem as the fringe field on the magnet causing the H$^-$ secondary ion beam to exit the magnet off the plane defined by the other secondary ions. We have identified potential solutions that would

allow more reliable quantification in the future. For this set of initial analyses, we believe the $H^-$/$^{12}C^-$ ratio is reliable.

One location was also imaged for $^{12}C^{13}C^-$ and $^{238}U^{16}O^-$ to confirm the presence of U in the large crystals. The count rates for $^{12}C^-$ and $^{12}C^{13}C^-$ are compared below for the same crystals to estimate the relative yield of these two species. This ratio was used to correct the $H^-$/$^{12}C^-$ ratios for our initial quantification estimates, discussed below.

Secondary ion image processing was performed using custom software (LIMAGE, L. Nittler, Carnegie Institution of Washington) that enables image alignment, ion ratio calculation, and extraction of quantitative data.

Quantification of absolute concentrations of H was estimated using published atom-per-atom relative sensitivity factors (RSFs) for $H^-$ and $C^-$ in silicon ($5 \times 10^{23}$ and $5 \times 10^{22}$ cm$^{-3}$; Wilson et al., 1989). These RSFs indicate that the yield of $H^-$ is lower than the yield of $C^-$ on an atom-per-atom basis. Because we need to use the relative yield of $H^-$ to $C^-$ to quantify the H content, we take the ratio of these RSFs to get an estimate of the relative useful yield (RUY) for the $H^-$/$C^-$, yielding $RUY_{H^-/C^-} = 10$, which reflects the lower yield of $H^-$ relative to $C^-$. This RUY can be used to estimate the atom-per-atom abundance of H relative to C in the sample with the following equation:

$$H/C = (^1H^-/^{12}C^-)_{SIMS}\ RUY_{H^-/C^-}\ F_{12C}/F_{1H,}$$

where $(^1H^-/^{12}C^-)_{SIMS}$ is the ion ratio determined in the SIMS analysis, $F_{12C}$ and $F_{1H}$ are the relative abundances of these isotopes, and H/C is the relative elemental ratio on an atom-per-atom basis in the sample. It is important to note that H/C does not directly reflect the concentration of H in the sample, but that it can be used to estimate the concentration of H in the sample if the concentration of C is known using the following equation:

$$[H] = [C]\ H/C$$

Typically, the concentration of the reference element is determined independently. Using this approach, concentration estimates are typically accurate to within a factor of two. Here, because we currently lack direct measurements of the C content, we assume the C concentration based on $UC_x$.

As discussed in the Results below, given an unexpectedly high yield of $C_2^-$ relative to $C^-$ from the $UC_x$ crystals, we adjust these calculations to reflect the yield of C as $C_2^-$. This adjustment was made by multiplying the RUY by the factor $^{12}C^-/[2 \cdot ^{12}C^{13}C^-/(2 \cdot F_{12C}\ F_{13C})]$, where $(2 \cdot F_{12C}\ F_{13C})$ reflects the relative abundances of the $^{12}C^{13}C^-$ species compared to the $^{12}C_2^-$, and the factor of 2 reflects the number of carbon atoms in $^{12}C_2^-$. While the sum of the species comprised of a particular element has previously been used for quantification, this specific adjustment to the RUY is not experimentally verified. Our justification is that this adjustment

provides more reasonable results than not making this adjustment, and it is rational given that the reference RSFs are based on a higher yield of C than H, and the highest yield for C is in the form of the dimer. Obviously, these numbers are provided as a starting point, and standards will be necessary to reliably determine H concentrations.

Post-analysis, crater depth was measured using a Dektak profilometer, and imaging was performed with an FEI Inspect scanning electron microscope (SEM) with energy dispersive X-ray analysis capability. X-ray spectra were collected to confirm that the large blocky crystals were $UC_x$.

## Results

Nine areas were sputtered for NanoSIMS analysis, and six yielded useful secondary ion data. All locations were used for the sputter rate calculations. In addition, we attempted analysis of one of the FIB craters with minimal pre-analysis sputtering and found that it had very low secondary ion yields. We moved to fresh surfaces to test the need for pre-analysis sputtering and did not return to the FIB craters. Significant pre-analysis sputtering was necessary before secondary ion yields stabilized and surface absorbed H and O were removed, revealing the material composition. All regions in this study were sputtered to a depth of at least 500nm before collecting data (Fig. 3). As shown in Fig. 3, subsequent sputtering and imaging would enable three-dimensional characterization of the sample and its inclusions.
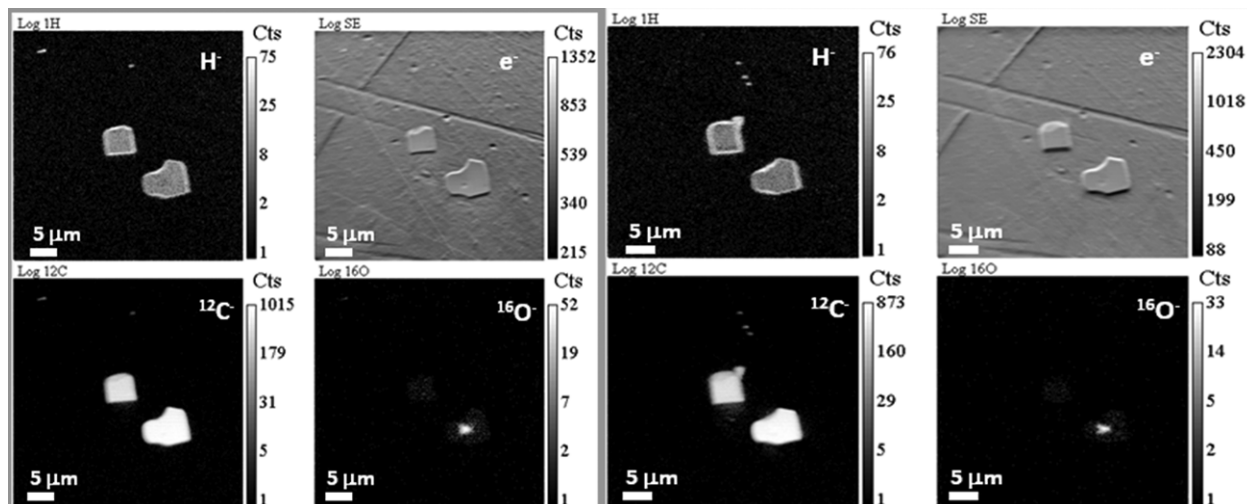


**Figure 3. Serial NanoSIMS images of a 50 x 50 $\mu m^2$ region of U metal after sputtering to depths of 0.5μm (left) and 1μm (right). The images are typical of others collected in this study both in the co –occurrence of H with C and the abundance of small inclusions. The $^{12}C^-$ image shows two large $UC_x$ crystals and a few small inclusions. The second set of images (right) show the potential for serial sputtering and analysis to understand the three dimensional distribution of H in these samples. The images are log-scale to enable the low-count-rate small and large inclusions to be visualized together.**

As suggested by the optical images (Fig. 2), the NanoSIMS secondary ion images show that the sample has large $UC_x$ inclusions (>3μm). These have high $C^-$ yields relative to the U metal (Fig. 3). We confirmed that these inclusions contain U by NanoSIMS and SEM X-ray

6

analysis. These large inclusions also have high $H^-$ yields relative to the U metal. Typically, the $H^-$ count rates at the margin of the crystals are higher than in the center (Fig. 4). The data suggest variability in the composition of the $UC_x$ rims. In Fig. 4, the rims appear to contain C because the $C^-$ and $H^-$ counts start to rise together and the $H^-$ counts peak a couple beam widths before the $C^-$ counts peak. However, in other $UC_x$ inclusions, the $H^-$ counts peak before the $C^-$ counts have risen significantly at all. In others, there is no H-rich rim.

After significant pre-analysis sputtering (>1μm depth), $O^-$ was primarily detected in imperfections in the $UC_x$ crystals (e.g., Fig. 3 & 5). We have insufficient data at this point to comment on low-level $O^-$ counts from some of the large $UC_x$ crystals. $O^-$ counts vary with both pre-analysis sputtering conditions and the primary beam current.
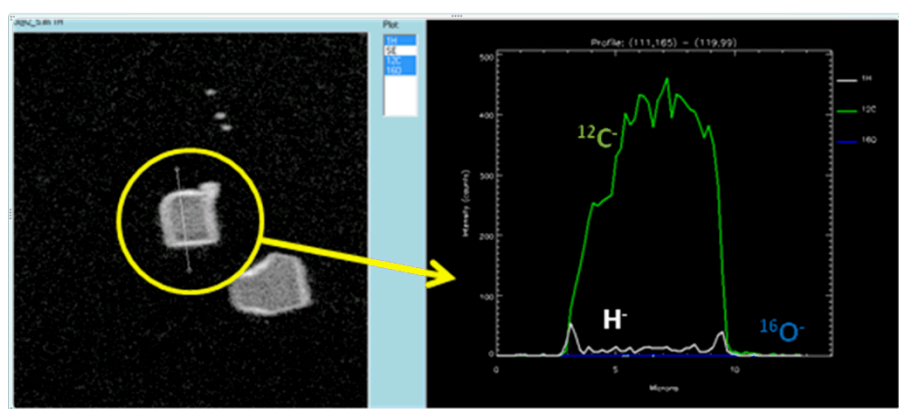


Figure 4. NanoSIMS $H^-$ ion image (left) and $H^-$, $C^-$ and $O^-$ line profile (right) across a $UC_x$ crystal (left center) from the area in Fig. 3. Note the prominent rim of H.

In addition to the large $UC_x$ inclusions, the NanoSIMS images show that the sample has ~1 μm and smaller inclusions that contain both H and C above the background level in the U metal (Fig. 3 & 5). $H^-$ and $C^-$ are correlated in these small inclusions (Fig. 6). O is not correlated with these small inclusions. As shown in the NanoSIMS images, these inclusions appeared to aggregate at that tens-of-micron scale. They also appear to aggregate at the 100s-of-micron scale, as indicated by significant variations in their abundance among the analysis regions. In the 50 x 50 $\mu m^2$ area in Fig. 3, two small inclusions are present in the first analysis, and three are present in the second analysis. In another 50 x 50 $\mu m^2$ region, no small inclusions were observed (Table 1). In the 90 x 90 $\mu m^2$ area imaged in Fig. 5, approximately 100 small inclusions are present. The preliminary estimate of their occurrence is a median of 10 per 100 x100 $\mu m^2$ and an average of 27 per 100 x100 $\mu m^2$. However, the number of analyses in this study is not sufficient to develop a model of the distribution of these small inclusions, and this wide range in observations makes any overall estimates of the abundance of these small inclusions highly uncertain. Note that the delineation of these small inclusions when they occur in large numbers is imprecise because the inclusions occur close to each other, the resolution of these analyses is limited, and the range in shapes observed does not allow a single search image to be imposed, but given the variability from region to region, this uncertainty is a small part of the overall uncertainty.

The NanoSIMS images indicate that some of the small inclusions are isometric (or point-like) and others are more linear. We do not have sufficient data to determine if the inclusions that appear isometric are actually ends of more linear features. Likewise, the linear features could be veins or the edges of other shapes. Serial analyses, as demonstrated in Fig. 3, could provide more definitive information on the morphology of these small inclusions. Also, these images do not have high enough lateral spatial resolution to determine if the features that are apparently linear are actually isometric inclusions close together. Higher resolution images or TEM imaging could address this question.
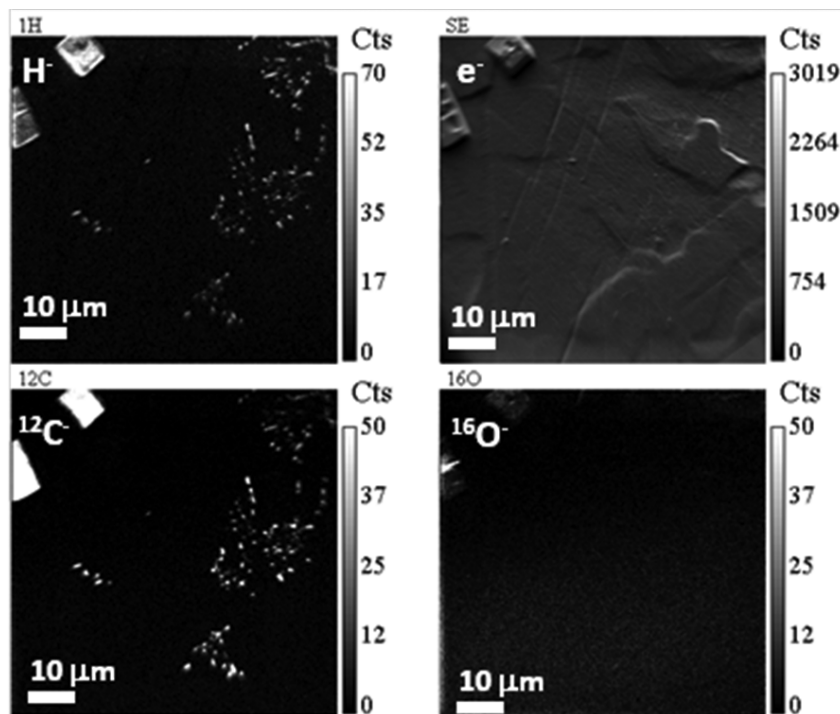


Figure 5. NanoSIMS images of a 90 x 90 $\mu m^2$ region of U metal after sputtering to a depth of 4.8$\mu m$. The $^{12}C^-$ image shows two large UC$_x$ crystals and the distribution of small inclusions. The data show the correlation between H and C in the sample (see Fig. 6). Scaling is set to above saturation for some regions to make the correlation easier to see. The secondary electron image (e$^-$) shows sample morphology. O is primarily in an imperfection in one of the large UC$_x$ crystals.

| Area # | Analysis current (pA) | Analysis raster (um) | Number of small inclusions | Density (N/100 x 100 um2) |
|---|---|---|---|---|
| A5 | | | | |
| A6 | 3 | 90 | 2 | 2.5 |
| A7 | 15 | 90 | 100 | 123.5 |
| A8 | 15 | 90 | 11 | 13.6 |
| A10 | 15 | 90 | 7 | 8.6 |
| A12 | 15 | 50 | 0 | 0.0 |
| A13 | 15 | 50 | 3 | 12.0 |

Table 1. Data by analysis area for the occurrence of H-bearing inclusions.

| | |
|---|---|
| Median | 10.3 |
| Average | 26.7 |
| Weighted average | 32.9 |
| N | 6 |

At the scale of individual small inclusions, it is difficult with this current data set to interpret the nature of the association of H and C. With our software, we are able to extract line profiles for the secondary ion count rate across inclusions (e.g., Fig. 7). In most cases, the H and C counts rise and fall together. However, there is some evidence for the H traces often being slightly broader than the C trace, indicating a slightly higher concentration of H around the
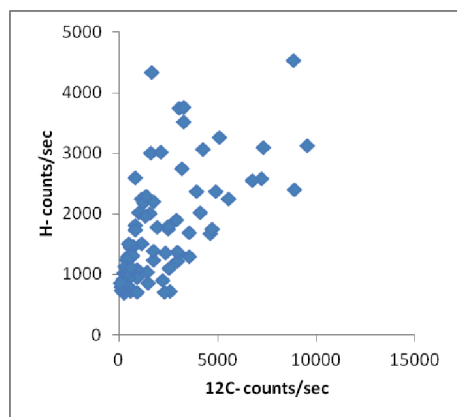
small inclusion. But only in one instance did we find an indication of H counts being higher at the edge of an inclusion than in the middle (Fig. 7, left), and this was a line profile across a linear set of inclusions. Higher resolution NanoSIMS images would potentially provide more insight into the association of C and H in these small inclusions. At this point, the data indicate that any compositional zoning in the small inclusions is minimal, and therefore, we treat these small inclusions as a single phase in our subsequent analyses in this report.
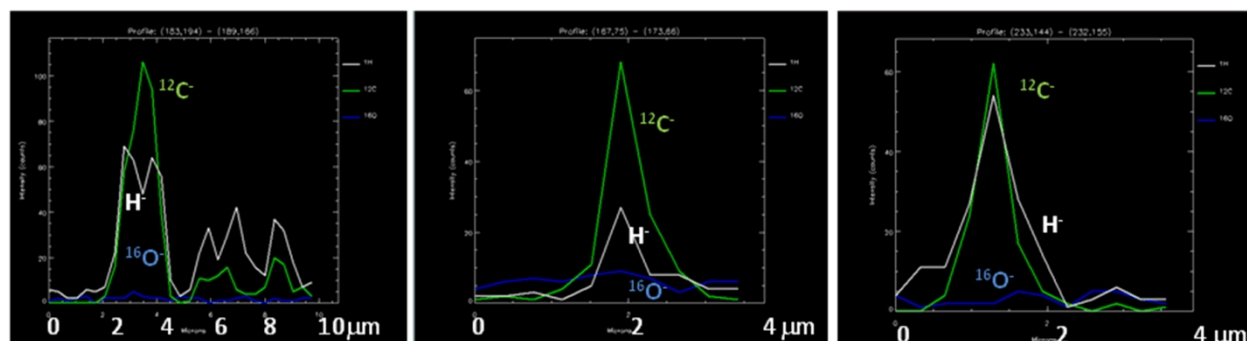


**Figure 7. H⁻, C⁻ and O⁻ line profiles across small inclusions in Fig. 5. The left scan is one of the few that indicates that H is more abundant at the edges of small inclusions. This is a line profile defined along series of inclusions. The other two are more typical of the result for ~1μm inclusions.**

*Quantification*

SIMS can be used for relative and absolute quantification. In this study, we can compare the relative abundance of H and C in the rims, large and small inclusions using the $^{1}H^{-}/^{12}C^{-}$ ratio to determine if they are compositionally similar. However, we do not currently have a solid basis for absolute quantification of the concentration of H in these samples. To quantify trace elemental composition with SIMS, it is necessary to (1) measure the ion ratio of the element of interest to a reference species, (2) know the absolute concentration of the reference species in the areas of interest, and (3) know the SIMS relative sensitivity factors for the two species. In this study, C⁻ is used as the reference ion for quantification because U⁻ has a very low yield and UO⁻ yield was only measureable in the inclusions. With C⁻ as the reference ion, it is necessary to

know its concentration, which we can only estimate in the case of the $UC_x$ crystals, which can only be UC, $U_2C_3$ or $UC_2$. In the case of the small inclusions, we do not know the primary phase, and therefore we do not have a basis for estimating the concentration of C in the small inclusions. Finally, we do not have matrix matched standards with which to determine the relative sensitivity factors for $H^-$ and $C^-$ in the phases in this study. Therefore, to provide preliminary data, we use published sensitivity factors and make adjustments that appear directionally reasonable, but which are almost certainly inaccurate (see below).

Relative quantification of the SIMS data indicates that the H in the U metal resides in three compositionally distinct phases. As a group, the small inclusions have higher $H^-$ yield relative to $C^-$ (or $H^-/C^-$ ratio) than the interiors of the large inclusions (Fig. 8, Table 2). The $H^-/C^-$ ratio in the small inclusions varies from 0.2 to 13, based on 93 small inclusions from all areas, compared to 0.005 to 0.5 in the interiors of 16 large inclusions. The median $H^-/C^-$ ratio for the small inclusions is 1.1 compared to 0.02 for the large inclusions. By contrast, the $H^-/C^-$ ratio in the rims of the large inclusions range from similar to the $H^-/C^-$ ratio in the interior to greater than the $H^-/C^-$ ratio in the small inclusions. $H^-/C^-$ ratios up to 100 were observed.

Based on these relative composition data, the small inclusions and the $UC_x$ rims are compositionally distinct from the $UC_x$ crystals. It does not seem likely that the 50 to 5,000 fold differences in the $H^-/C^-$ ratios could be accounted for by $UC_x$ that contain higher H concentrations in the crystal lattice. Therefore, it seems likely that the small inclusions and the $UC_x$ rims contain $UH_3$, most likely intermixed with $UC_x$, unless there is some mixed UCH phase.
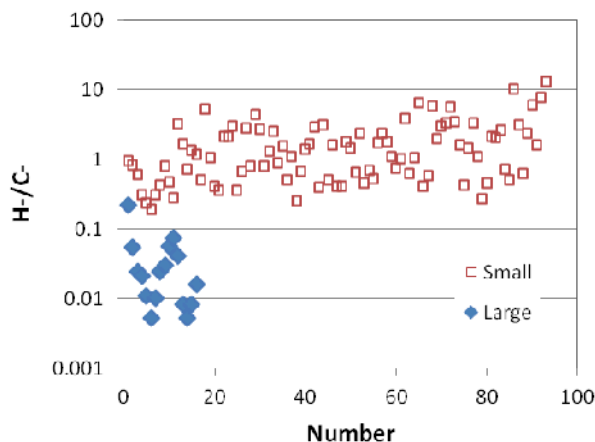


Figure 8. $H^-$ to $C^-$ ion ratio for large and small inclusions in U metal. Cumulative data are in Table 2.

| | Median $^1H^-/^{12}C^-$ | Average $^1H^-/^{12}C^-$ | SD | SE | N |
|---|---|---|---|---|---|
| Large inclusions | 0.023 | 0.038 | 0.053 | 0.013 | 16 |
| Small inclusions | 1.10 | 1.87 | 2.09 | 0.22 | 93 |

Table 2. $H^-$ to $C^-$ ion ratio statistics for large and small inclusions in U metal in Fig. 10. SD = standard deviation; SE = standard error; N = number of analyses.

Absolute quantification in these samples is significantly more complicated than we initially expected. In the absence of matrix matched standards, we estimated the relative useful yield (RUY) for H relative to C using published relative sensitivity factors (RSFs) for silicon. Normally, this approach would yield a RUY within approximately a factor of two of the "true" value. However, in this case, we found that this approach gave wildly unrealistic concentrations for H in the $UC_x$ crystals. Based on the published RSFs, the approximate H/C ratio in these samples is calculated to be ~10 times the $^{1}H^{-}/^{12}C^{-}$ ion ratio, or 0.05 to 5 for the interiors of the $UC_x$ inclusions. Taking this further, assuming the inclusions are $UC_2$, the median H abundance would be ~15% on an atom-per-atom basis, and considering the mass of H relative to U and C, the $UC_x$ inclusions would be ~600 ppm H by weight. These concentrations appear much too high.

We posit that the primary reason that these estimates are too high is that the most abundant ion species that carbon is forming from the $UC_x$ in these samples is $C_2^{-}$. The $C_2^{-}/C^{-}$ ratio is ~28, which incidentally is very different from what we observe in SiC samples. Given this particular result, it is unlikely that the $C^{-}$ monomer could have the same yield relative to $H^{-}$ as observed in silicon, which would yield significantly more $C^{-}$ monomer than $C_2^{-}$. Therefore, we applied the adjustment factor $^{12}C^{-}/[2\cdot^{12}C^{13}C^{-}/(2\cdot F_{12C} F_{13C})]=0.018$ to $RUY_{H-/C-}$, as discussed in the Methods. Using this adjusted RUY, the approximate H/C ratio in the $UC_x$ inclusions is calculated to be 0.0009 to 0.09. Assuming the inclusions are $UC_2$, the median H abundance would be ~0.28% on an atom-per-atom basis, and considering the mass of H relative to U and C, the $UC_x$ inclusions would be ~10 ppm H by weight. These estimates still seem too high, but they are directionally more plausible than the estimates without the $^{12}C^{-}/[2\cdot^{12}C^{13}C^{-}/(2\cdot F_{12C} F_{13c})]$ adjustment. Again, standards will be necessary given the unusually high yield of $C_2^{-}$ from these inclusions.

As discussed above, because we do not know the composition of the small inclusions or the rims, we cannot make concentration estimates. While our adjusted $RUY_{H-/C-}$ indicates that the H/C atom-per-atom ratio in these features approaches or exceeds 1, indicating that they could contain $UH_3$, we will have to await better standards to provide reliable insight on the topic of the phases in which H resides in these samples.

*Inclusion identification for other analyses*

One approach to better characterizing the small inclusions and the $UC_x$ rims would be to use the NanoSIMS to locate inclusion of interest and then characterize them using electron beam analysis. The electron beam characterization could be done with electron microprobe wavelength dispersive X-ray analysis, which could be done with the intact sample, or the FIB could be used to extract electron-transparent sections for transmission electron microscopy (TEM) electron diffraction analysis. This step should be relatively straight forward because the small inclusions can be identified post-NanoSIMS analysis using SEM. Correlated NanoSIMS and

SEM images show that the H- and C-rich small inclusions are associated with topographical features that are visible in the NanoSIMS secondary electron images and SEM images (Fig. 9). Though small, they are sufficient guide for follow-up analysis. The primary risk is that oxidation during preparation for other analyses could transform the phases of interest. However, our initial experience is that the sputter craters oxidize imperceptibly compared to the polished U metal surface, presumably because Cs passivates the U metal surface. Our initial attempt to characterize the mineralogy of the small inclusions with the SEM was inconclusive because of the interference of U X-rays at the C line.
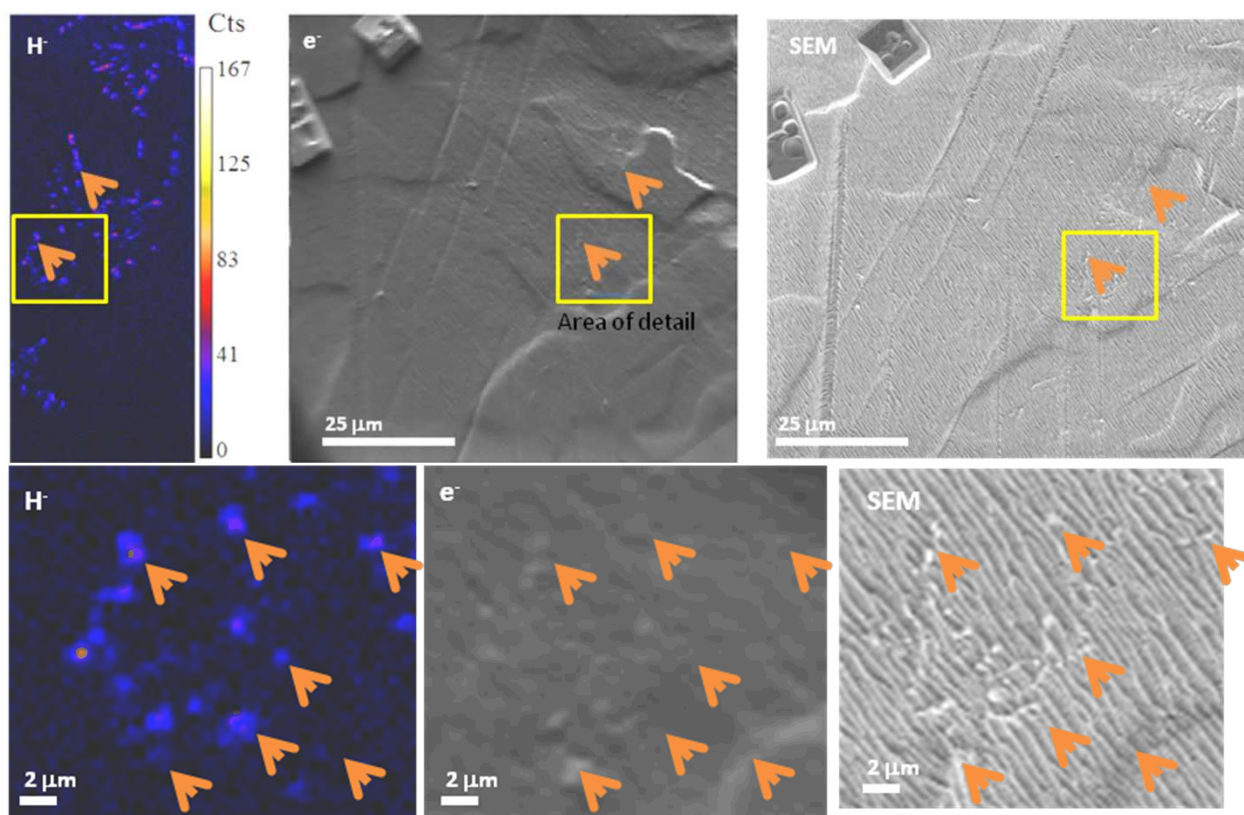


Figure 9. Comparison of NanoSIMS H- and secondary electron images with post-analysis SEM imaging from Fig. 4, showing the location of small features that correlate with higher H- counts. The lower panels show the area of detail in the upper panel. These features could be the target of FIB lift-out sectioning and TEM analysis. Note that the NS image is slightly distorted relative to reality, and therefore the SEM image of the area is somewhat elongated.

*Sputter rate*

The sputter rates for the U metal and $UC_x$ crystals were determined using the areas sputtered for this study (Table 3). The profilometer provided depth data for all sputtered craters, but depth to the $UC_x$ crystals was harder to obtain with our single-scan profilometer, and only 3 were measured so far. Our sputter rate estimates are based on the volume of material removed (depth in nm and area in $\mu m^2$) with a measured $^{133}Cs^+$ primary beam current

(pA) for a given duration (s). Therefore we use the practical units of $\mu m^2$ nm $pA^{-1}$ $s^{-1}$. These estimates can be converted to atoms removed per incident ion, if desired.

The sputter rate of the U metal is nearly twice the sputter rate for $UC_x$. We estimate the sputter rate for U metal to be 1.28±0.078 $\mu m^2$ nm $pA^{-1}$ $s^{-1}$, (mean±standard error) and for $UC_x$, ~0.66±0.03 $\mu m^2$ nm $pA^{-1}$ $s^{-1}$. For comparison, we estimate the sputter rate for bacterial spores to be ~2 $\mu m^2$ nm $pA^{-1}$ $s^{-1}$, and viruses and cells to be ~1 $\mu m^2$ nm $pA^{-1}$ $s^{-1}$. As can be seen in Table 3, there were outlying points for the sputter rate measurements, which are potentially just the result of inaccurate accounting of the sputtering time or current. Determining the sputter rate was not the top priority of these analyses, and with the long duration of sputtering necessary to remove >1μm of material from large areas combined with some logistical and technological issues, outliers would not be surprising. Nonetheless, the U metal data raise the possibility of a systematic issue, and it would improve confidence in the data to perform more controlled sputtering experiments. Also, it would improve confidence to make more measurements for $UC_x$ crystals.

| Area # | Sputter current (pA) | Duration (hr) | Nominal raster size (um) | Measured raster area (um2) | Depth (nm) | Sputter rate (um2 nm/pA /s) | Material | Depth (nm) | Sputter rate (um2 nm/pA /s) | Material |
|---|---|---|---|---|---|---|---|---|---|---|
| A5 | 370 | 11 | 100 | 9,540 | 1,200 | 0.87 | U | | | |
| A6 | 1000 | 6 | 100 | 11,300 | 2,600 | 1.36 | U | 877 | 0.60 | UCx |
| A7 | 1000 | 12.5 | 110 | 12,600 | 4,800 | 1.34 | U | | | |
| A8 | 1000 | 18 | 110 | 11,500 | 7,500 | 1.33 | U | | | |
| A9 | 1000 | 5 | 100 | 11,136 | 2,750 | 1.53 | U | 1273 | 0.71 | UCx |
| A10 | 370 | 8.5 | 100 | 9,975 | 1,500 | 1.32 | U | | | |
| A10 | 370 | 13.5 | 40 | 1,600 | 9,071 | 0.81 | U | | | |
| A11 | 370 | 10.5 | 60 | 3,528 | 5,779 | 1.45 | U | | | |
| A12 | 370 | 4.5 | 60 | 3,420 | 2,485 | 1.50 | U | | | |
| A13 | 1000 | 1 | 60 | 3,933 | 1,168 | 1.28 | U | 629 | 0.69 | UCx |
| | | | | | Median | 1.34 | U | Median | 0.69 | UCx |
| | | | | | Average | 1.28 | U | Average | 0.66 | UCx |
| | | | | | SE | 0.08 | U | SE | 0.03 | UCx |
| | | | | | N | 10 | U | N | 3 | UCx |

Table 3. Data for sputter rate of U metal and $UC_x$ for 16kV $^{133}Cs^+$. Note that corrections are made to the data for sputter crater distortion. U metal sputter rate is based on average crater depth, excluding inclusions. $UC_x$ sputter rate is based on local crater depth.

## Summary

This study has demonstrated the association of H with C in U metal. This association holds in micron-scale $UC_x$ crystalline inclusions and smaller, micron- and sub-micron scale inclusions of unknown composition. The morphological and compositional data indicate that

the small and large inclusions are two distinct populations. Morphologically, the small and large inclusions are distinct in size and shape. The absence of inclusions that bridge the size and morphology gap between the two types of inclusions supports the idea that these are two distinct populations. Also, compositionally the large and small inclusions have distinct H/C ratios. Possibly the rims of the large inclusions are compositionally similar to the small inclusions, but at this point the data indicate that they too are distinct. The relative compositional data in this study provide tentative evidence that the small inclusions and $UC_x$ rims identified in this study include $UH_3$ intermixed with $UC_x$. Further analysis will be necessary to provide definitive data on the H-containing phases in this sample.

**Reference cited:**

Powell, G. L. 2007. Hydrogen in uranium. Depleted Uranium Conference, Knoxville, TN, April 23-25, 2007.

Wilson, R. G., Stevie, F. A. and Magee, C. W. 1989. Secondary Ion Mass Spectrometry: A Practical Handbook for Depth Profiling and Bulk Impurity Analysis. Wiley, New York.